Vacancy healing as a desorption tool: Oxygen triggered removal of stored ammonia from NiO_{1-x}/MOR validated by experiments and simulations

James M. Crawford[1], Ryther Anderson[1], Ryan J. Gasvoda[1], Nolan C. Kovach[2], Courtney S. Smoljan[1], Jacek B. Jasinski[3], Brian G. Trewyn[2], Sumit Agarwal[1], Diego A. Gómez-Gualdrón[1], Moises A. Carreon[1,*]

[1]Chemical and Biological Engineering Department, Colorado School of Mines, 1613 Illinois St., Golden, CO 80401, United States of America.

[2]Department of Chemistry, Colorado School of Mines, 1500 Illinois St., Golden, CO 80401, United States of America.

[3]Conn Center for Renewable Energy Research, University of Louisville, Lutz Hall 010, 200 East Shipp Street Walk, Louisville, KY 40292, United States of America

Keywords: zeolite confinement, gas storage, oxygen vacancy, metal oxide, carbon-free fuel

ABSTRACT: Gas storage via adsorption in microporous crystals, such as zeolites, has the potential to transform both the energy and transportation sectors. This potential results from the highly tunable pore chemistry and geometry of zeolites, which allows for precise control of the chemical environment of the adsorbed gas. However, while strong gas-solid interactions are desirable to maximize gas storage capacity, they hinder the effective release of the stored gas species. In the current work, the partial reduction of a nickel-oxide/zeolite nanocomposite led to a remarkable heat release upon exposure to air, which was attributed to the exothermic healing of oxygen vacancies in the NiO_{1-x} lattice. This heating effect was reproducible over at least 10 treatments and was compared to different types of porous supports, providing evidence that uniform micropores and an optimal pore size is required to obtain the observed heating properties. We demonstrate that this heating phenomena can be applied to the desorption of hysteretic ammonia, leading to 38 % desorption of the chemisorbed gas without the need for external heating or pressure swing.

INTRODUCTION

Ammonia storage is of great interest as a carbon-free fuel and as a high density hydrogen carrier.[1,2] Targets set by the US Department of Energy (DOE) for the storage of hydrogen require a sorbent material with highly reversible storage capacities (1500 cycles), low cost (333 \$ kg^{-1} H_2), fast kinetics (1-5 min), full exposure to sunlight, and ambient operating temperatures (-40-60 °C).[3] Storage of ammonia in solid sorbents meets many of these H_2 storage requirements and offers benefits including hazard mitigation, minimal pressurization and cooling requirements, and facile material handling.[4,5] One major challenge in gas storage is the efficient release of chemisorbed gas species.[6] Strong adsorption can result in hysteresis, hindering gas release. Current gas desorption techniques include vacuum/pressure and temperature swing, ultraviolet/visible light exposure,[7,8] and solvent extraction.[6,9] While these technologies offer potentially feasible unit operations for large scale applications, DOE hydrogen storage targets largely eliminate light exposure (must tolerate sunlight throughout storage, handling, and transportation), temperature swing (operation temperatures below 60 °C), and vacuum/pressure swing (high operation and maintenance costs modulating between 1 and 0.01 bar) as desorption candidates.

Zeolites, microporous tetrahedrally coordinated aluminosilicate crystals, have shown large capacities, high stability, and prolonged retention of ammonia but require moderate to high temperatures for desorption.[10] Metal oxides with unique intrinsic heating properties have recently gained major attention. Nagaoka and coworkers demonstrated the oxidative reforming of hydrocarbons using partially reduced CeO_2 supported catalysts, which exhibited heating upon exposure to oxygen.[11–13] Their work highlights the possibility of instilling triggered heating properties into solid state materials.

In the present work, we synthesized a partially reduced zeolite-supported NiO_{1-x} nanocomposite that undergoes a reversible exothermic reaction on exposure to air, reaching temperatures as high as 694 °C. The nanocomposite material displayed reproducible performance, evidenced by 10 consecutive cycles where temperatures above 550 °C were recurrently observed. This heating phenomenon results primarily from the rapid repopulation, or healing, of oxygen vacancies formed during thermal reduction of the NiO_{1-x} lattice. We compare the effect of different supports and demonstrate that pore size and pore uniformity impact the maximum observed temperature and relaxation time. Finally, we show that this unique heating phenomenon can promote desorption of strongly chemisorbed ammonia, providing an alternative tool for the rational design of gas storage materials.

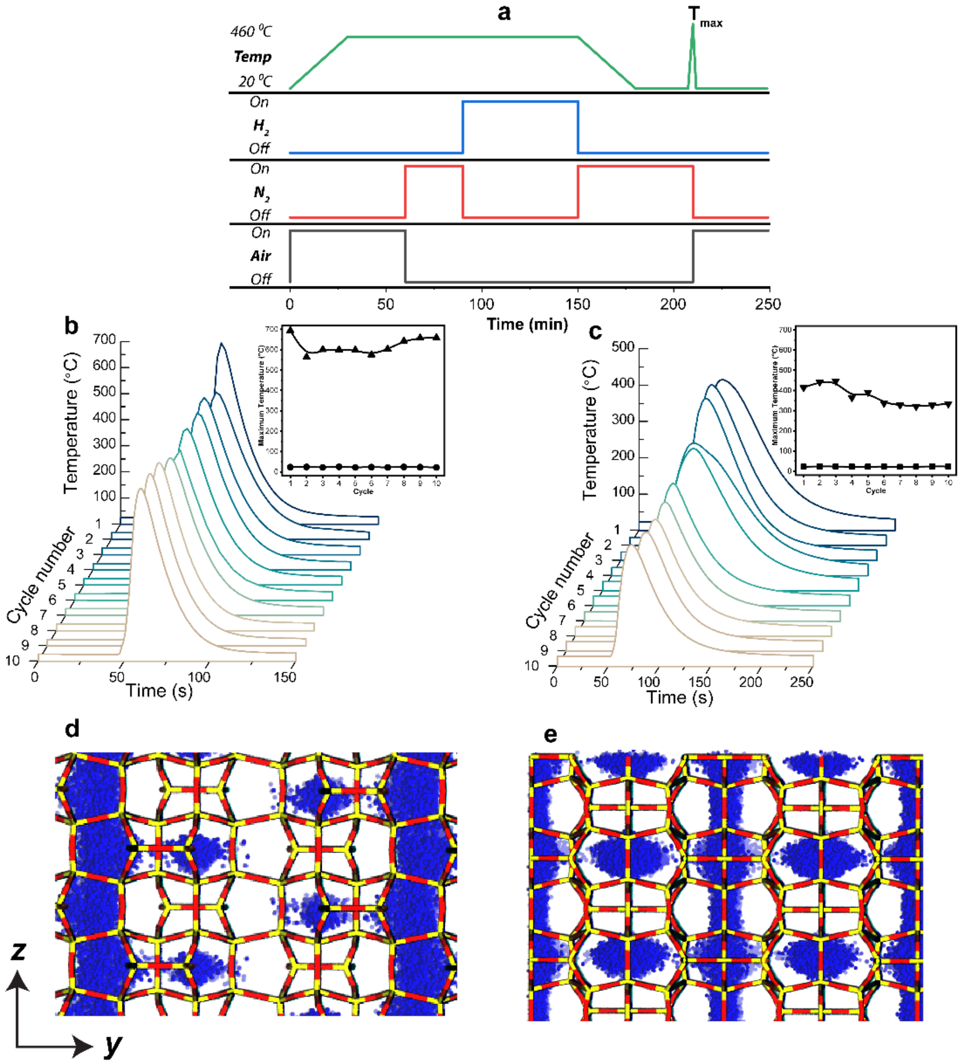

Figure 1. a) Process diagram for the calcination, reduction, purge, cooling, and air triggered heating of Ni nanocomposites. Temperature profiles over 10 cycles for b) Ni/MOR and c) Ni/FER. Insets represent the maximum temperatures for each cycle: Ni/MOR (▲), MOR (●), Ni/FER (▼), FER (■). Oxygen diffusion snapshots from MD simulations in d) MOR and e) FER.

RESULTS AND DISCUSSION

Zeolite mordenite (MOR) was selected as a porous support for nickel as it offers preferential cation exchange sites near the pore mouth of the main channel.[14,15] Ni/MOR was prepared *via* ion exchange synthesis from NH_4-MOR using a basic, concentrated, aqueous solution of nickel nitrate (Figure S1). Ion exchange synthesis was chosen because it offers the controlled incorporation of metal ions within the zeolite pore.[16,17] The obtained material was calcined in flowing air at 460 °C for 1 h, purged with N_2 at 460 °C for 30 min, reduced in flowing H_2 at 460 °C for 1 h, purged again with N_2 at 460 °C and finally cooled to room temperature under N_2 (**Figure 1**a). After the thermal pretreatments and upon exposure to air, a remarkable heating event was observed using a K-type thermocouple. As Ni/MOR was exposed to repeated calcinations, reductions, and reactions with air, high temperatures were recurrently observed, showing no obvious trend of degradation with a maximum temperature of 694 °C (Figure 1b). Typical relaxation times, or the time required for the sample to cool from the maximum observed temperature to half of the maximum temperature ($t_{\text{relax}} = t_{\frac{1}{2}T_{\max}} - t_{T_{\max}}$), for Ni/MOR samples were between 10-20 s, indicating a rapid release of heat.

Comparing MOR, FER, and AC supports

Temperature profiles obtained from Ni/MOR prompted us to determine if this exothermic response was exclusive to the combination of Ni on MOR, or if this phenomenon was observed on other porous supports. To answer this question, zeolite ferrierite (FER) and activated carbon (AC) were evaluated as inorganic and organic porous analogs, respectively. Using the same ion exchange synthesis and thermal treatment described for Ni/MOR, temperature profiles for Ni/FER (Figure 1c) and Ni/AC were obtained. The Ni/FER sample exhibited temperature profiles similar in shape to those observed for Ni/MOR, but with a longer relaxation time of 20-40 s and a maximum temperature of 447 °C. It is interesting to compare the responses of Ni/FER and Ni/MOR as both samples had nearly the same Si/Al ratio, Ni loading, dispersion, and degree of reduction (Table S1). The major difference between the two zeolites (besides topology) is the primary pore size. We hypothesized that the smaller primary 10-membered ring (MR) in FER (4.3 x 5.5 Å) resulted in slower oxygen diffusion as compared to the 12-MR in MOR (6.7 x 7 Å). This hypothesis was tested using molecular dynamics (MD) calculations wherein the self-diffusion coefficients for oxygen were measured in MOR and FER frameworks (Figure S2-4, Table S2). Diffusion of oxygen in both MOR and FER was dominated by displacement in the z-direction (Figure 1d, e). Oxygen diffused through FER slower than in MOR, with total diffusion coefficients of 6.6×10^{-5} and 1.0×10^{-4} cm^2 s^{-1}, respectively. Therefore, a plausible reason for the slower relaxation time and lower maximum temperature observed in Ni/FER as compared to Ni/MOR is this difference in diffusion coefficients. Ni/AC yielded a relaxation time of 45 s and a non-uniform temperature profile with three pronounced peaks and a maximum temperature of 222 °C (Figure S5). Unfortunately, the Ni/AC system experienced mass loss upon cycling, so further studies were halted.

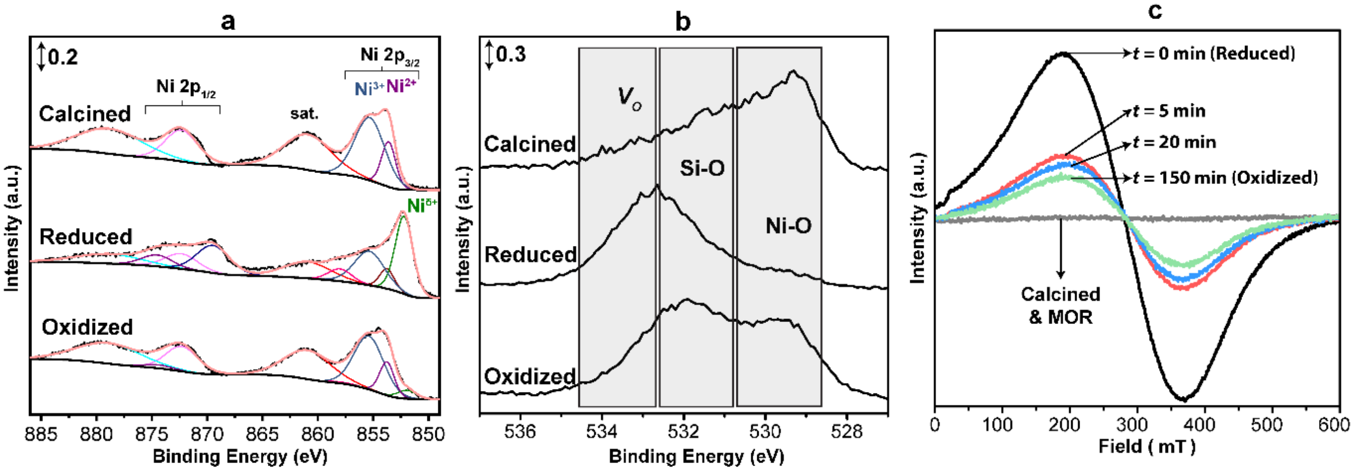

Figure 2. Characterization of the calcined, reduced, and oxidized sample by a) XPS Ni 2p spectrum, b) O 1s spectrum, and c) room temperature EPR spectrum.

Characterization of the primary Ni/MOR oxidative states

To better understand the central cause of the observed heat release for Ni/MOR, further characterization was required. We focused our study on the three primary oxidative states of Ni/MOR including the calcined, reduced, and the oxidized sample after exposure to air. Characterization included powder X-ray diffraction (PXRD) to elucidate the crystalline structure, X-ray photoelectron spectroscopy (XPS) to understand the changes in chemical composition, and electron spin paramagnetic resonance spectroscopy (EPR) to provide information about the defects formed during the reduction.

PXRD showed the characteristic MOR pattern along with the expected NiO phase in the calcined sample (Figure S6). The oxidized sample showed the presence of NiO and Ni phases. The Ni 2p spectrum obtained from XPS showed that the calcined sample was primarily composed of NiO, 853.7, 855.4, 860.9, 865.6 eV[18] (**Figure 2**a) as expected from PXRD. The reduced sample gave a shift towards metallic Ni, 852.6 eV,[19] but still contained NiO species. The large reduction in the shake-up satellite at 860.9 eV in the reduced sample is indicative of a partially reduced surface.[20,21] After exposure to air, the oxidized sample shifted to higher binding energy where the dominant species was NiO with only a small contribution from metallic Ni. Additionally, upon exposure to air, the shake-up satellite was regained. The O 1s spectrum showed dramatic changes between the calcined, reduced, and oxidized samples (Figure 2b). It is important to note that the O 1s region shows a combination of both NiO and support oxide moieties overlapping, which prevented detailed deconvolution. Generally, the O 1s region in metal oxides exhibits an asymmetric shift towards higher binding energy as the ratio of metal to oxygen increases and non-stoichiometric states occur.[20,22] The calcined sample showed a strong Ni-O response at 529 eV,[18] as expected. The calcined sample also showed only a weak shouldering of the Si-O peak at 532 eV[23] due to Ni-O coverage of the support. This observation is also evidenced in the survey spectrum, where the characteristic Si-O sp^2 signal was not observed in the calcined sample (Figure S7). Additionally, the calcined sample did not exhibit a significant response in the 533 eV region attributed to loosely bound surface species or oxygen vacancies.[22,24] In the oxidized sample, we observed a Si-O response at 532 eV,[23] due to morphology changes in surface Ni-O coverage. A strong contribution from Ni-O was evident in the oxidized sample, similar to the calcined sample. Another important feature of the oxidized sample was the tailing into the 533 eV region indicating that some loosely bound surface species or oxygen vacant sites remained after exposure to air. The reduced sample showed a negligible contribution from Ni-O, a modest contribution from Si-O, and a major contribution from oxygen vacancies or surface species around 533 eV. The observed changes in the O 1s and Ni 2p spectra in the reduced sample are indicative of a non-stoichiometric, partially reduced NiO surface.[25] These results indicate that exposure to air promoted the oxidation of the non-stoichiometric Ni.

Characterization of oxygen vacancies in Ni/MOR

It has been documented that the formation of oxygen vacancies in NiO under H_2 flow takes place at temperatures between 400-460 °C,[26] matching our selected reduction parameters. Using density functional theory with the Hubbard Hamiltonian (DFT+ U), the formation energy of an oxygen vacancy in the NiO lattice was calculated to be 4.30 eV (Table S3). Room temperature EPR results (Figure 2c) show a broad response typical of partially reduced Ni supported on zeolites, centered around ~290 mT with a g-value of 2.06.[27,28] The large broad peak in the reduced sample is attributed to the promotion of oxygen vacancies due to the thermal reduction of Ni with hydrogen.[29] This claim is further evidenced as the MOR support and the calcined Ni/MOR sample exhibited no EPR response as expected[27,30] and in agreement with the O 1s spectrum from XPS. When NiO is nearly stoichiometric, antiferromagnetic spin states largely eliminate the EPR signal. The reduced sample, with no exposure to air, showed the largest EPR response. EPR spectra collected at 5, 20, and 150 min (oxidized) after exposure to air display a rapid initial decrease followed by a plateau in vacancy concentration over time as defects are healed by oxygen. These findings are corroborated by the observations from XPS and highlight the rapid nature of vacancy occupation in NiO_{1-x} lattice. The effective oxygen uptake of the reduced sample, measured by O_2 titration at 35 °C, was 0.294 mmol g^{-1} (Figure S8, Table S1). By comparing this value with the theoretical amount of O_2 required to completely oxidize Ni^0/MOR to NiO/MOR with a metal loading of 8.9 % (0.758 mmol g^{-1}), we calculated the stoichiometry of the reduced sample to be $NiO_{0.61}$/MOR $\left(1 - x = 1 - \frac{O_2\ consumed}{O_2\ theory}\right)$ following the method described by Sato et al.[13]

Locating confined and surface Ni species on MOR

Argon isotherms were collected for the parent MOR and oxidized Ni/MOR and compared to GCMC-simulated isotherms in four blocked-pore models: no pore blocking and blocking of the small, medium, and large MOR pores. When adsorption occurs in ordered porous materials, a step is observed in quantity of gas adsorbed when new pores begin to fill. The kinetic diameter of Ar (0.34 nm) makes it an ideal candidate to probe the various pores of MOR. We were able to match the key characteristics of our experimental isotherm using linear combinations of the simulated Ar isotherms in these blocked-pore models, providing insights into the most likely locations for Ni inside the pore (Figure S8-10, Video S1). A comparison of the experimental and computational isotherms is provided in **Figure 3.** From this analysis, it was found that Ni was most prevalent in the medium pore (~70% of these pores blocked), which is consistent with the high concentration of proton exchange sites at this location.[14]. Additionally, Ni was found to be located in the large pore (~30% of these pores blocked). We hypothesize that the confined Ni nanoparticles may be contributing to the sustained heating activity in the Ni/MOR sample across multiple cycles.

Imaging of the calcined and oxidized Ni/MOR surface revealed considerable morphological shifts (**Figure 4**). From the high-resolution transmission electron microscopy (HRTEM) images, the lattice spacing of both MOR (0.58 nm) and NiO (0.21 nm) are observed in the calcined sample. Selective area electron diffraction (SAED) confirmed the existence of these phases in the calcined Ni/MOR sample. Scanning transmission electron microscopy coupled with high angle annular dark field (STEM-HAADF) imaging and energy-dispersive X-ray spectroscopy (STEM-EDS) provided a clear distribution of the Ni species across the MOR surface in the calcined sample. In the

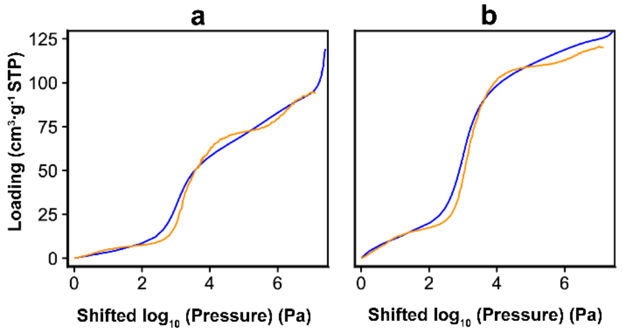

Figure 3. Experimental (blue) and simulated (orange) Ar isotherm (-186 °C) for a) Ni/MOR and b) parent-MOR.

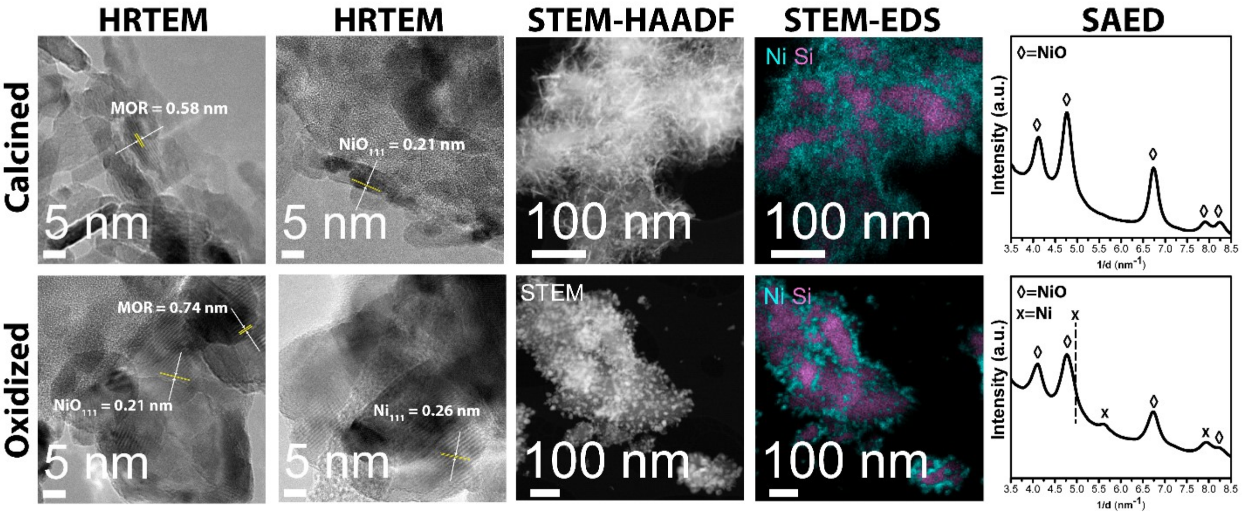

Figure 4. Transmission electron microscopy analysis of the (top) calcined and (bottom) oxidized Ni/MOR. In the order from left to right: HRTEM images, STEM-HAADF images, STEM-EDS elemental maps, and intensity profiles of SAED patterns.

oxidized sample, SAED and HRTEM provided evidence that both Ni and NiO moieties are present across the MOR support. STEM-HAADF images show a drastic change in structure from needle-like morphologies in the calcined sample to clusters of Ni across the support surface in the oxidized sample. The Ni agglomerates are likely to have formed due to coalescence or Ostwald ripening during the thermal reduction. The change in Ni surface coverage observed in the STEM-HAADF images and STEM-EDS elemental maps agrees well with the coverage observations from XPS, where Si 2s and 2p peaks are absent in the calcined sample and present in the oxidized sample.

We have shown evidence that the thermal reduction step with hydrogen resulted in the promotion of active oxygen vacancies in the Ni-O lattice on Ni/MOR. The support material provided a high surface area template for both surface and confined Ni species which were likely found in the medium and large pores of MOR as supported by GCMC calculations. The greater pore size in MOR as compared to FER promoted faster diffusion of oxygen to the vacant sites as supported by MD simulations, yielding a more pronounced heat release. While particle agglomerates formed during the thermal treatments, the macroscopically observed maximum temperature of Ni/MOR was stable over 10 repeated treatments.

Vacancy healing of Ni/MOR for NH_3 desorption

To test the functionality of Ni/MOR as an adsorbent with intrinsic heating properties, we turned to ammonia as our probe molecule. Record NH_3 capacities, reported by Dincă and coworkers, exceeded 19 mmol NH_3 g^{-1} sorbent.[5] The vast majority of high uptake materials are metal-organic frameworks (MOF) with open metal sites. However, desorption of ammonia from MOF materials remains a challenge due to the chemisorption of NH_3 on these sites. We found that oxidized Ni/MOR had an STP loading of 4.15 mmol NH_3 g^{-1} with a hysteretic gas release at low pressure due to chemisorption (**Figure 5**a). Using NH_3 temperature programmed desorption (TPD) with an *in situ* calcination/reduction pretreatment similar to that used in the cycling studies, we measured the amount of ammonia adsorbed to

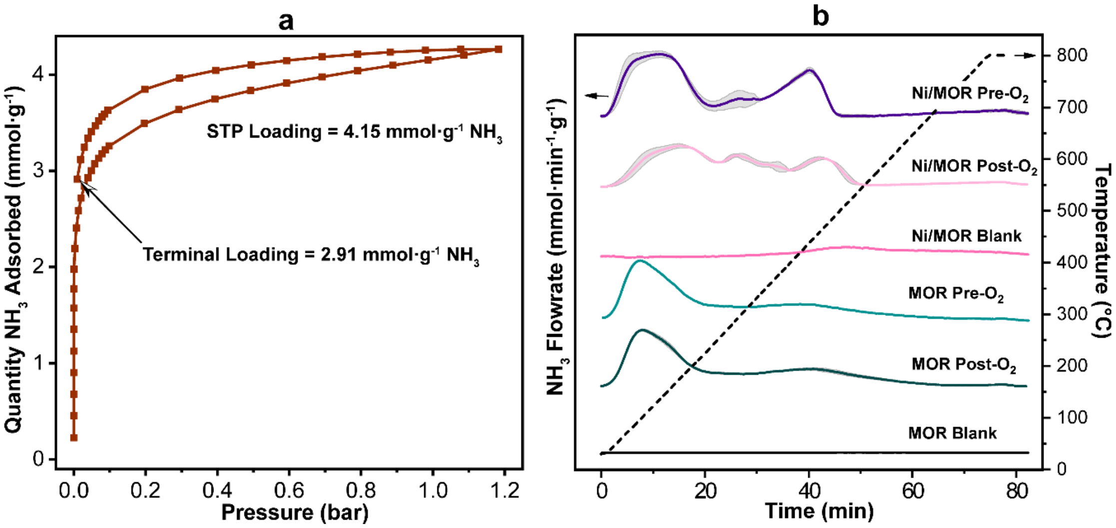

Figure 5. a) NH_3 isotherm measured at 25 °C for Ni/MOR. b) NH_3-TPD profiles for MOR and Ni/MOR pre and post-oxygen exposure. The shaded regions represent the standard deviation around the average of triplicate data sets.

the reduced Ni/MOR sample at STP. Without exposure to oxygen, Ni/MOR retained 5.39±0.23 mmol NH_3 g^{-1} sorbent (Figure 5b). Upon exposure to flowing oxygen for 5 min, as dictated by the DOE target for gas delivery rates, the Ni/MOR sample retained 3.33±0.14 mmol NH_3 g^{-1} sorbent. This indicates that the oxygen exposure step resulted in the removal of 38.3% of the chemisorbed NH_3. Using the parent MOR as a control, we observed an ammonia removal of less than 1% due to oxygen exposure, indicating that the vacancy healing and intrinsic heating properties of Ni/MOR promoted the desorption. The possibility of NH_3 decomposition or oxidation over Ni/MOR was ruled out by tracking the temperature and gas composition during the TPD experiment (Figure S11 and S12). To gain a perspective on this removal efficiency a comparison was made with current state-of-the-art ammonia sorbent materials (**Table 1).**

Table 1. Comparison to the state-of-the-art NH_3 sorbent materials.

Ref.	Sample	Material	Removal Method	Uptake[a)]	Terminal Loading[b)]	Desorbed[c)]
				[mmol NH_3·g^{-1}]	[mmol NH_3·g^{-1}]	[%]
[31]	MFM-300(Al)	MOF	ΔP	13.9	4.6	67
[2]	BPP-5	POP	ΔP	17.7	8.1	54
[2]	BPP-7	POP	ΔP	16.0	7.9	51
[32]	NU-300	MOF	ΔP	8.3	3.7	55
[33]	Co-(BTDD)	MOF	ΔP	12.0	4.4	63
[33]	Ni-(BTDD)	MOF	ΔP	12.0	5.7	53
[33]	Mn-(BTDD)	MOF	ΔP	15.5	7.5	52
[5]	Ni-(BBTA)	MOF	ΔP	14.7	10.1	31
[5]	Cu-(BBTA)	MOF	ΔP	19.8	14.7	26
[5]	Co-(BBTA)	MOF	ΔP	18.0	13.1	27
[34]	$Co(NA)_2$	MOF	ΔP	17.4	13.0	25
[34]	$Zn(NA)_2$	MOF	ΔP	10.1	9.6	5
[34]	$Cu(NA)_2$	MOF	ΔP	13.4	13.0	3
[34]	$Cd(NA)_2$	MOF	ΔP	6.0	6.0	0
[35]	H/Y [d)]	ZEO	ΔP	5.4	1.1	80
[35]	Co/Y [d)]	ZEO	ΔP	8.6	1.6	81
[35]	Cu/Y [d)]	ZEO	ΔP	9.3	2.9	69
This Work	Ni/MOR	ZEO	IH	5.4[e)]	3.3[e)]	38
	Ni/MOR	ZEO	ΔP	4.2	2.9	30

[a)] Uptake at 25 °C/1 bar. [b)] NH_3 loading of the desorption branch at P = 0.01 bar estimated from published NH_3 isotherms. [c)] (Uptake-Terminal Loading)/Uptake·100. [d)] Measured at 54 °C/0.4 bar. [e)] Calculated from NH_3-TPD. Metal-organic framework (MOF), porous-organic polymer (POP), zeolite (ZEO), vacuum swing (ΔP), intrinsic heating (IH).

The desorption efficiency from intrinsic heating falls within typical values for vacuum swing technologies of other porous materials. In addition, the intrinsic heating effect out preforms vacuum swing desorption for Ni/MOR. DFT calculations were conducted for the binding energy of NH_3 on NiO and NiO + O vacancy (Figure S13 Table S4). This analysis revealed that the lowest energy configuration for NH_3 on NiO + O-vacancy is centered above Ni and that the O-vacancy was slightly repulsive to NH_3. Therefore, oxygen would have space to dissociate and heal the O-vacancy site, generating enough heat (-4.30 eV) to overcome the binding energy of NH_3 on the NiO lattice (-0.56 eV), NH_3 on the NiO + O-vacancy lattice (-0.60 eV), NH_3 on Brønsted acid sites within MOR (-2.44 eV).[36], NH_3 diffusion barriers along the z-direction in MOR (0.04 eV) (Figure S4), and NH_3 diffusion on the NiO (100) surface (0.59 eV) (Figure S14). We also found that increased temperature did not have a large effect on the MOR heat capacity (Figure S15).

CONCLUSIONS

In summary, we have demonstrated that the partially reduced Ni-zeolite nanocomposite Ni/MOR displays reproducible exothermic heating properties on exposure to air. When pretreated, the sample can be loaded with 5.39 mmol NH_3 g^{-1} at STP. A NH_3 removal efficiency of 38.3% was found on exposure to oxygen which was largely a result of the intrinsic heating properties instilled in the material. The desorption efficiency for Ni/MOR *via* intrinsic heating was higher than that observed from vacuum swing desorption. *In silico* experiments were used to model the probable location of the Ni species within the zeolite pore, the diffusion of O_2 and NH_3 within the zeolite pore, the O-vacancy formation energy in NiO, and the theoretical binding environment of NH_3 on NiO + O vacancy. The intrinsic heating phenomenon in Ni/MOR provides an effective and novel desorption technology that could offer a low cost, minimal on-site energy input, and recyclable NH_3 storage solution. This work illustrates a proof-of-concept for employing intrinsic heating in metal-zeolite nanocomposites for the effective desorption of ammonia. Further investigations of different metal/support combinations may lead to higher ammonia uptakes and improved desorption properties provided by intrinsic heating.

ASSOCIATED CONTENT

Supporting Information

The supporting information is available free of charge via the Internet at http://pubs.acs.org. Synthetic and computational details, Figures S1-S14, Video S1, Tables S1-S4

AUTHOR INFORMATION

Corresponding Author

*E-mail: mcarreon@mines.edu

Author Contributions

The manuscript was written through contributions of all authors. All authors have given approval to the final version of the manuscript.

ACKNOWLEDGMENT

J.C. acknowledges the National Science Foundation Graduate Research Fellowship Program NSF-GRFP Award #1000271688 for partial financial support of this work. M.C. thanks the National Science Foundation NSF-CBET Award # 1705675 for financial support of this work. D.G. acknowledges financial support from NSF-CBET Award #1921484.

ABBREVIATIONS

REFERENCES

(1) Chakraborty, D.; Damsgaard, C. D.; Silva, H.; Conradsen, C.; Olsen, J. L.; Carvalho, H. W. P.; Mutz, B.; Bligaard, T.; Hoffmann, M. J.; Grunwaldt, J. D.; et al. Bottom-Up Design of a Copper–Ruthenium Nanoparticulate Catalyst for Low-Temperature Ammonia Oxidation. *Angew. Chemie - Int. Ed.* **2017**, *56* (30), 8711–8715.

(2) Van Humbeck, J. F.; McDonald, T. M.; Jing, X.; Wiers, B. M.; Zhu, G.; Long, J. R. Ammonia Capture in Porous Organic Polymers Densely Functionalized with Brønsted Acid Groups. *J. Am. Chem. Soc.* **2014**, *136* (6), 2432–2440.

(3) US Department of Energy. DOE Technical Targets for Onboard Hydrogen Storage for Light-Duty Vehicles www.uscar.org (accessed Feb 27, 2020).

(4) Klerke, A.; Christensen, C. H.; Nørskov, J. K.; Vegge, T. Ammonia for Hydrogen Storage: Challenges and Opportunities. *J. Mater. Chem.* **2008**, *18* (20), 2304–2310.

(5) Rieth, A. J.; Dincă, M. Controlled Gas Uptake in Metal–Organic Frameworks with Record Ammonia Sorption. *J. Am. Chem. Soc.* **2018**, *140* (9), 3461–3466.

(6) Morris, R. E.; Wheatley, P. S. Gas Storage in Nanoporous Materials. *Angew. Chemie - Int. Ed.* **2008**, *47* (27), 4966–4981.

(7) Xu, J.; Zhou, X.; Gao, Z.; Song, Y. Y.; Schmuki, P. Visible-Light-Triggered Drug Release from TiO2 Nanotube Arrays: A Controllable Antibacterial Platform. *Angew. Chemie - Int. Ed.* **2016**, *55* (2), 593–597.

(8) Šutka, A.; Järvekülg, M.; Gross, K. A.; Kook, M.; Käämbre, T.; Visnapuu, M.; Trefalt, G.; Šutka, A. Visible Light to Switch-on Desorption from Goethite. *Nanoscale* **2019**, *11* (9), 3794–3798.

(9) Song, Z.; Nambo, A.; Tate, K. L.; Bao, A.; Zhu, M.; Jasinski, J. B.; Zhou, S. J.; Meyer, H. S.; Carreon, M. A.; Li, S.; et al. Nanovalved Adsorbents for CH4 Storage. *Nano Lett.* **2016**, *16* (5), 3309–3313.

(10) Puértolas, B.; Veses, A.; Callén, M. S.; Mitchell, S.; García, T.; Pérez-Ramírez, J. Porosity-Acidity Interplay in Hierarchical ZSM-5 Zeolites for Pyrolysis Oil Valorization to Aromatics. *ChemSusChem* **2015**, *8* (19), 3283–3293.

(11) Nagaoka, K.; Sato, K.; Fukuda, S.; Nakashiki, S.; Nishiguchi, H.; Lercher, J. A.; Takita, Y. Oxidative Reforming of n -Butane Triggered by Spontaneous Oxidation of CeO 2− x at Ambient Temperature. *Chem. Mater.* **2008**, *20* (13), 4176–4178.

(12) Nagaoka, K.; Sato, K.; Takita, Y. Effect of the Nature of Rhodium Catalyst Supports on Initiation of H 2 Production during N-Butane Oxidative Reforming at Room Temperature. *J. Catal.* **2012**, *287*, 86–92.

(13) Sato, K.; Adachi, K.; Takita, Y.; Nagaoka, K. Effect of the Nature of the CeO 2 Support of the Rh Catalyst on Triggering the Oxidative Reforming of n -Butane for H 2 Production from Ambient Temperature. *ChemCatChem* **2014**, *6* (3), 784–789.

(14) Grundner, S.; Markovits, M. A. C.; Li, G.; Tromp, M.; Pidko, E. A.; Hensen, E. J. M.; Jentys, A.; Sanchez-Sanchez, M.; Lercher, J. A. Single-Site Trinuclear Copper Oxygen Clusters in Mordenite for Selective Conversion of Methane to Methanol. *Nat. Commun.* **2015**, *6* (1), 7546.

(15) Veefkind, V. A.; Smidt, M. L.; Lercher, J. A. On the Role of Strength and Location of Brønsted Acid Sites for Ethylamine Synthesis on Mordenite Catalysts. *Appl. Catal. A Gen.* **2000**, *194–195*, 319–332.

(16) Wang, N.; Sun, Q.; Yu, J. Ultrasmall Metal Nanoparticles Confined within Crystalline Nanoporous Materials: A Fascinating Class of Nanocatalysts. *Adv. Mater.* **2019**, *31* (1), 1–23.

(17) Liang, J.; Liang, Z.; Zou, R.; Zhao, Y. Heterogeneous Catalysis in Zeolites, Mesoporous Silica, and Metal–Organic Frameworks. *Adv. Mater.* **2017**, *29* (30), 1–21.

(18) Mansour, A. N. Characterization of NiO by XPS. *Surf. Sci. Spectra* **1994**, *3*, 231–238.

(19) Biesinger, M. C.; Payne, B. P.; Lau, L. W. M.; Gerson, A.; Smart, R. S. C. X-Ray Photoelectron Spectroscopic Chemical State Quantification of Mixed Nickel Metal, Oxide and Hydroxide Systems. *Surf. Interface Anal.* **2009**, *41* (4), 324–332.

(20) McKay, J. M.; Henrich, V. E. Surface Electronic Structure of

NiO: Defect States, O2 and H2O Interactions. *Phys. Rev. B* **1985**, *32* (10), 6764–6772.

(21) van Veenendaal, M. A.; Sawatzky, G. A. Nonlocal Screening Effects in 2 p X-Ray Photoemission Spectroscopy Core-Level Line Shapes of Transition Metal Compounds. *Phys. Rev. Lett.* **1993**, *70* (16), 2459–2462.

(22) Gao, R.; Li, Z.; Zhang, X.; Zhang, J.; Hu, Z.; Liu, X. Carbon-Dotted Defective CoO with Oxygen Vacancies: A Synergetic Design of Bifunctional Cathode Catalyst for Li-O2 Batteries. *ACS Catal.* **2016**, *6* (1), 400–406.

(23) Jensen, D. S.; Kanyal, S. S.; Madaan, N.; Vail, M. A.; Dadson, A. E.; Engelhard, M. H.; Linford, M. R. Silicon (100)/SiO 2 by XPS. *Surf. Sci. Spectra* **2013**, *20* (1), 36–42.

(24) Sexton, B. A.; Hughes, A. E.; Turney, T. W. An XPS and TPR Study of the Reduction of Promoted Cobalt-Kieselguhr Fischer-Tropsch Catalysts. *J. Catal.* **1986**, *97* (2), 390–406.

(25) Roberts, M. W.; Smart, R. S. C. The Defect Structure of Nickel Oxide Surfaces as Revealed by Photoelectron Spectroscopy. *J. Chem. Soc. Faraday Trans. 1* **1984**, *80* (11), 2957–2968.

(26) Rodriguez, J. A.; Hanson, J. C.; Frenkel, A. I.; Kim, J. Y.; Pérez, M. Experimental and Theoretical Studies on the Reaction of H2 with NiO: Role of O Vacancies and Mechanism for Oxide Reduction. *J. Am. Chem. Soc.* **2002**, *124* (2), 346–354.

(27) Stöcker, M.; Tangstad, E.; Aas, N.; Myrstad, T. Quantitative Determination of Ni and V in FCC Catalysts Monitored by ESR Spectroscopy. *Catal. Letters* **2000**, *69* (3–4), 223–229.

(28) Simon, M. W.; Bennett, C. O.; Suib, S. L. Cyclopropane Reactions over Brønsted, Cation, and Metal Sites in Ni/NaX Zeolites. *J. Catal.* **1994**, *148* (1), 100–112.

(29) Li, Y.; Zhao, Y.; Chen, B.; Wang, W. Synergetic Catalysis of Nickel Oxides with Oxygen Vacancies and Nickel Phosphide for the Highly Efficient Hydrodeoxygenation of Phenolic Compounds. *ChemCatChem* **2018**, *10* (12), 2612–2619.

(30) Ghosh, A. K.; Kevan, L. Electron Spin Resonance Studies of Ethylene Dimerization Catalyzed by Nickel Species on Y Zeolites. *J. Phys. Chem.* **1990**, *94* (7), 3117–3121.

(31) Godfrey, H. G. W.; da Silva, I.; Briggs, L.; Carter, J. H.; Morris, C. G.; Savage, M.; Easun, T. L.; Manuel, P.; Murray, C. A.; Tang, C. C.; et al. Ammonia Storage by Reversible Host-Guest Site Exchange in a Robust Metal-Organic Framework. *Angew. Chemie* **2018**, *130* (45), 14994–14997.

(32) Chen, Y.; Zhang, X.; Ma, K.; Chen, Z.; Wang, X.; Knapp, J.; Alayoglu, S.; Wang, F.; Xia, Q.; Li, Z.; et al. Zirconium-Based Metal–Organic Framework with 9-Connected Nodes for Ammonia Capture. *ACS Appl. Nano Mater.* **2019**, *2* (10), 6098–6102.

(33) Rieth, A. J.; Tulchinsky, Y.; Dincă, M. High and Reversible Ammonia Uptake in Mesoporous Azolate Metal–Organic Frameworks with Open Mn, Co, and Ni Sites. *J. Am. Chem. Soc.* **2016**, *138* (30), 9401–9404.

(34) Chen, Y.; Shan, B.; Yang, C.; Yang, J.; Li, J.; Mu, B. Environmentally Friendly Synthesis of Flexible MOFs M(NA) 2 (M = Zn, Co, Cu, Cd) with Large and Regenerable Ammonia Capacity. *J. Mater. Chem. A* **2018**, *6* (21), 9922–9929.

(35) Liu, C. Y.; Aika, K. ichi. Ammonia Adsorption on Ion Exchanged Y-Zeolites as Ammonia Storage Material. *J. Japan Pet. Inst.* **2003**, *46* (5), 301–307.

(36) Niwa, M.; Suzuki, K.; Katada, N.; Kanougi, T.; Atoguchi, T. Ammonia IRMS-TPD Study on the Distribution of Acid Sites in Mordenite. *J. Phys. Chem. B* **2005**, *109* (40), 18749–18757.

SYNOPSIS TOC: Heat generation inside porous zeolite mordenite is promoted by exothermic oxygen vacancy healing in the NiO_{1-x} lattice. This heating phenomena is demonstrated to be an effective tool in the removal of chemisorbed ammonia, which typically requires temperature or vacuum swing. When compared to other porous supports, mordenite is shown to provide topographical benefits that result in optimal heating and 38% removal of ammonia.

Insert Table of Contents artwork here

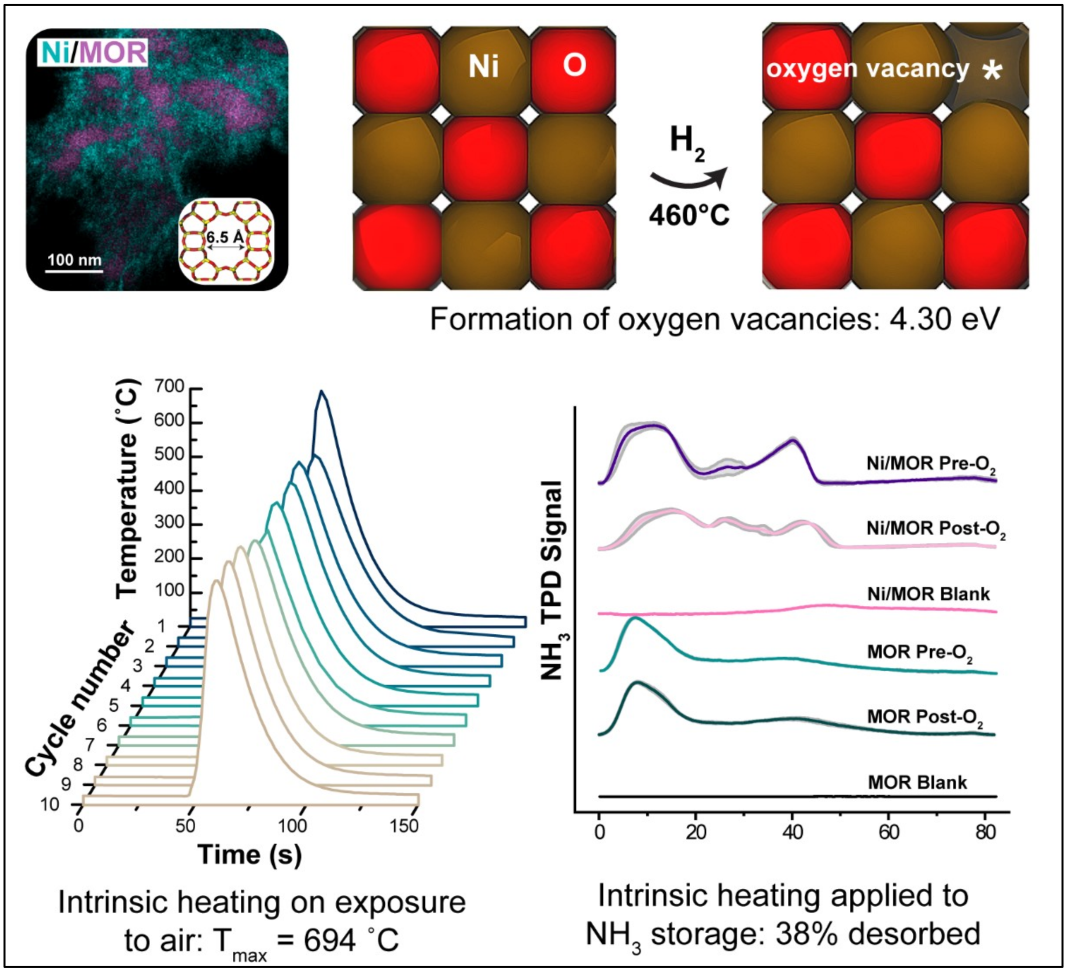

Formation of oxygen vacancies: 4.30 eV

Intrinsic heating on exposure to air: T_{max} = 694 °C

Intrinsic heating applied to NH_3 storage: 38% desorbed